Pore-scale spatiotemporal dynamics of microbial-induced calcium carbonate growth and distribution in porous media

Na Liu [a,*], Malin Haugen [a], Benyamine Benali [a], David Landa-Marbán [b], Martin A. Fernø [a,b]

[a] *Department of Physics and Technology, University of Bergen, Allégaten 55, Bergen 5007, Norway*
[b] *NORCE Norwegian Research Centre AS, Nygårdsgaten 112, Bergen 5008, Norway*

ABSTRACT

The naturally occurring bio-geochemical microbial-induced calcium carbonate precipitation (MICP) process is an eco-friendly technology for rehabilitating construction materials, reinforcement of soils and sand, heavy metals immobilization and sealing subsurface leakage pathways. We report pore-scale spatiotemporal dynamics of the MICP process in porous media, relevant for reduced environmental risk by leakage during CO_2 geological storage. Effects of hydrodynamics and supersaturation on the MICP with *Sporosarcina pasteurii* stains were studied using a high-pressure, rock-on-a-chip microfluidic device. Bacterial cell numbers and variation in cementation concentration controlled the crystal size and pore-scale distribution by influencing the local supersaturation. Local pore structure determined crystal nucleation, where low velocity regions tended to nucleate more crystals. $CaCO_3$ crystallization was observed at subsurface pressure (100 barg) with a reduced sealing performance due to the low microbial activity from elevated pressure. We identify that hydrodynamics and supersaturation determine crystal nucleation and growth in porous systems, providing important experimental evidence for subsurface environmental applications and validation of upscaled MICP models.

1. Introduction

Microbial-induced calcium carbonate precipitation (MICP) is a naturally occurring bio-geochemical process, considered as a potential plugging agent in many environmental and engineered applications (Mitchell et al., 2010; Ortega-Villamagua et al., 2020; Siddique and Chahal, 2011; Stocks-Fischer et al., 1999). For geological carbon dioxide (CO_2) sequestration, it is imperative to develop technologies that reduce the environmental risk from leakage of the sequestered CO_2 (Celia et al., 2005; Watson and Bachu, 2009). A range of fracture-sealing materials has been suggested for carbon geo-sequestration, including paraffin wax (Grisak et al., 1980), gels (Zaitoun et al., 2007), and cement (Nasvi et al., 2013). These synthetic materials, although proven successful, are often associated with high costs and may introduce hazardous substances to the environment. MICP can deliver calcium, urea and microbial strains – all natural components frequently found in the subsurface – far from the injection well to seal gas leakage pathways down to small aperture fractures (< 100 μm) (Phillips et al., 2016). In addition, MICP shows great potential to reduce near-wellbore permeability, remediating CO_2 related corrosion, and reduce undesirable migration of CO_2 or other fluids (Cunningham et al., 2013; Mitchell et al., 2009; Phillips et al.,

2013), without plugging the injection well (Landa-Marbán et al., 2021). Many bacterial species, naturally occurring in diverse environments including subsurface reservoirs, can produce urease enzymes for hydrolysis of urea that increase surrounding solution pH and alkalinity (Okyay et al., 2016). In the presence of calcium ions, this alkaline environment promotes chemical precipitation of $CaCO_3$, resulting in a significant reduction of porosity and permeability. Extracellular polymeric substances and suspended biomasses offer negatively charged functional groups for cation adsorption and provide nucleation sites for precipitation. Current knowledge predicts the distribution of biominerals and permeability reduction due to the MICP sealing (Cunningham et al., 2014; Phillips et al., 2016); models on carbonate mineral nucleation and its growth kinetics at different levels of complexity have been developed (Cunningham et al., 2018; Jimenez-Martinez et al., 2022; Weinhardt et al., 2022), with a satisfactory match between laboratory experiments and field observations. Detailed studies on the pore-scale spatiotemporal dynamics of the MICP process are lacking, and the influence of pore structure and operational parameters (i.e., pressure, cell number) on $CaCO_3$ precipitate size and polymorphs is largely unknown.

To our knowledge, there are a handful reported experimental pore-

---

* Corresponding author.
E-mail address: Na.Liu@uib.no (N. Liu).

scale studies of MICP for leakage pathway mitigation during geological CO_2 storage (Armstrong and Ajo-Franklin, 2011; Haugen et al., 2021). Reported kinetic studies are mainly on investigation of the MICP process relevance for soil stabilization (Lin et al., 2020) and heavy metals immobilization (Hu et al., 2021). Pore-scale properties of $CaCO_3$ precipitates, such as crystal size, morphology, and distribution in porous media can strongly affect the sealing efficiency and plugging strength. Kinetics of nucleation and growth of $CaCO_3$ crystals strongly relies on hydrodynamics and supersaturated state in the pore, which are influenced by pore structure and operational parameters (i.e., pressure, cell number) (Yoon et al., 2019).

We report new laboratory data that improve our understanding of the pore-scale kinetics of microbial induced $CaCO_3$ precipitation and distribution in porous media at different operational parameters. Our results shed light on $CaCO_3$ crystal size, frequency and distribution during MICP in the context of geological CO_2 storage, with emphasis on the influence of hydrodynamics and supersaturation. We study the morphological transformation of $CaCO_3$ in a single pore and quantify the pore-scale $CaCO_3$ crystal growth rate. We systematically evaluate the impact of pore structure and operational parameters on crystal size, frequency and distribution in porous media. Finally, we estimate the efficiency of the MICP based on the porosity reduction due to the precipitation of $CaCO_3$ in the pore network. We anticipate that our new results could improve understanding and predictability of porous MICP for different applications and aid the development of efficient upscaled MICP models.

2. Material and methods

2.1. Bacterial strain and nutrient solution

Sporosarcina pasteurii DSM 33 was used to produce urease for hydrolyzing urea $(CO(NH_2)_2)$ into ammonium (NH_4^+) and carbonate (CO_3^{2-}) ions in the aqueous phase. Table 1 lists properties of all the solutions used for experiments. After autoclaving, the nutrient solution (NS) was filtered through a syringe filter (0.20 μm of pore size, 514–0061, VWR) to avoid plugging injection channels. A dense bacterial solution (BS, 0.2 mL) was mixed with 10 mL of nutrient solution and precultured at 30 °C overnight. Figure S1 shows the optical density (OD_{600}) and pH measurements of the bacterial solution and nutrient solution during preculturing.

2.2. Microfluidic pore network and unit area

The pore network of micromodel (Fig. 1) was based on a thin section from a real sandstone rock sample. Modifications were made to improve the connectivity in 2D porous pattern, resulting in a higher 2D porosity and permeability (porosity = 0.61 and permeability = 2.97 Darcy) relative to the 3D sandstone sample. Micromodel production procedures can be found in (Buchgraber et al., 2012). The total micromodel pore volume (PV) is 11.10 μL. The porous pattern constitutes 36 (4 × 9) repetitions of a smaller unique pattern. There are four connection ports that allow injection and/or production of fluids, and two fluid distribution channels (200 μm width × 30 μm depth) that connect ports 1 and

2, and ports 3 and 4. The total area of the porous network is 26.95 × 22.50 mm; an area of interest (AOI) with the size 25.07 × 20.43 mm was used to improve image processing due to edge reflection. The AOI was split into 16 columns and 18 rows (288 units in total) for the image analysis, and a unit was defined (1.65 × 1.14 mm) to calculate local porosity and crystal density. The unique porous pattern contained 8 units (2 rows × 4 columns), with a porosity range between 0.59 and 0.66.

2.3. Experimental setup and procedure

The microfluidic device was fixed in a motorized scanning stage under a Zeiss microscope (Axio Zoom. V16, Zeiss) and illuminated with a cold-light (CL 9000 LED) source including a Diffuser S ring. This microscope setup was able to capture fluid flow and crystal growth in the whole pore network with a resolution of 4.38 μm/pixel. Pore space temperature (kept constant at 30 °C) was controlled by circulating warm water through internal copper tubes in the chip holder, and pressure was controlled by a high precision plunger pump (Quizix Q5000-10 K), and a back pressure regulator (EB1ZF1 Equilibar Zero Flow) connected to a pressurized 300 mL N_2 cylinder. Absolute pressure was measured by two pressure transmitters (ESI, APLISENS PRE-28 SMART) mounted on flow ports 1 and 4 with a measuring range of 0 - 2.50 barg and a static pressure limit of 250 barg. The experimental setup has a high-precision injection system with a constant dead-volume, including a two-position switch valve (Idex, 9725) and two 6-ports select valves (Idex, MXP7970–000). Bypass lines enabled cleaning of tubing and prevented mixing and reactions of BS and CS before entering the pore network.

The experimental procedure for microbial-induced $CaCO_3$ precipitation consists of the following 6 steps:

1. Preparation: The pore space was flushed with ethanol, deionized (DI) water and H_2O_2 (ACS reagent, 30 wt% solution in water, Thermo Scientific™) to clean all surfaces and wastes from previous experiments, followed by > 100 pore volumes (PVs) of DI water.
2. Pressurization: The microfluidic system was pressurized up to the operating pressure range from 19 to 100 barg by flowing DI water at 50 μL/min through the bypass with pressure communication with the pore network.
3. Nutrient solution: To remove residual water, approximately 20 PVs of NS were injected at 20 μL/min from port 3 to port 2, followed by 1 PV injection from port 3 to port 1.
4. Bacterial inoculation: For inoculation and bacterial attachment to the pore space surfaces, 10 PVs of BS $(OD_{600} = 0.86$ and pH = 9.51) were injected at 6 μL/min from port 3 to port 2.
5. Cleaning flow lines: To prevent carbonate precipitates clogging the inlet and outlet tubes, residual BS was removed from inlet and outlet tubes prior to injection of CS. Approximately 1 PV of NS was injected from port 1 to 2 to remove the residual bacterial solution in the channel connected to port 1.
6. Carbonate precipitation: CS was injected from port 1 to port 4 at 1 μL/min to precipitate calcium carbonate in the pore space. CS contains 0.5 M $CaCl_2$ and 0.5 M urea for the precipitation reaction. The volumetric flowrate corresponds to a Darcy velocity of 2.03 mm/min.

The spatiotemporal distribution of calcium carbonate precipitates was visualized by the high-resolution microscope system. All experiments were performed above 19 barg pore pressure to eliminate the produced gas bubbles from bacteria growth in the solution. Properties of pore network and experimental procedures are detailed elsewhere (Benali et al., 2022; Haugen et al., 2021; Song et al., 2018).

2.4. Image analysis and Raman spectroscopy

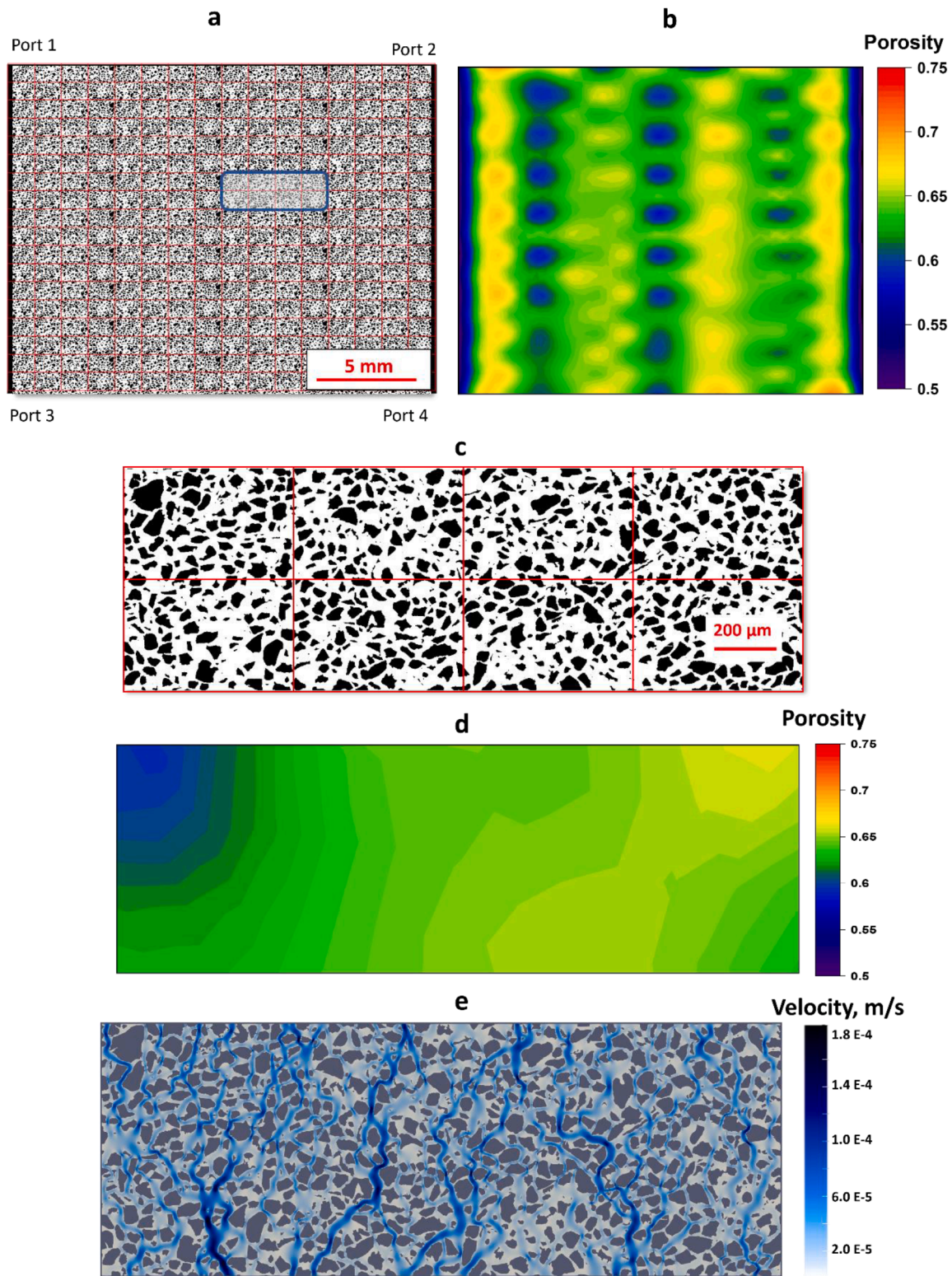Microscopic images were continuously acquired during calcium

Table 1
Summary of fluid properties.

Solutions	Composition	Concentration	pH
Nutrient solution (NS)	Brain heart infusion broth (BHI Broth, 53,286 Sigma-Aldrich)	4.70 wt%	7.41
	Urea (U5378, Sigma-Aldrich)	2.00 wt%	
Bacterial solution (BS)	*Sporosarcina pasteurii* stains (DSMZ GmbH supplier)	~10^9 cells/ mL	9.51
Cementation solution (CS)	Calcium chloride (calcium chloride dehydrate, 31,306, Sigma-Aldr.)	14.70 wt%	6.66
	Urea (U5378, Sigma-Aldrich)	6.00 wt%	

Fig. 1. (a) The binary image (Width × Height = 6028 pixels × 4665 pixels) of the AOI was split into 16 columns and 18 rows for local porosity calculation. Units are shown as red boxes, and the blue rectangle represents one unique porous pattern. Note that units on left and right sides have smaller size because of cropping edges of the image (68 pixels). (b) Contour plot of local porosity distribution in AOI. The contour lines are smoothed with a parameter of 9.84 E-4. (c) Binary image of a unique porous pattern (1.65 × 1.14 mm), with corresponding porosity distribution map in (d). (e) Simulation of steady-state flow velocity magnitude (confer to https://daavid00.github.io/pymm/examples.html#image for details on the simulation setup).

carbonate mineral growth. Acquisition time for the whole pore network (total 121 separate images) was 73 s, and images of the entire pore network were continuously captured during crystal nucleation and growth. The crystals were translucent in the original image and thresholding algorithms were applied to improve crystal size calculations (Figure S2). Local porosity change from crystal growth was quantified by dividing the horizontal area of crystals by the pore space in each unit. We assume that crystals fill the entire pore depth and crystal size equals to its horizontal area based on 2D segmented images, causing overestimate of crystal size and porosity reduction. After forming $CaCO_3$ precipitates in the pore network for 1 H, 4 H and 20 H, the microfluidic device was depressurized to ambient conditions and disconnected from the experimental setup for Raman spectroscopy tests. $CaCO_3$ precipitates at different stages in the pore network were analyzed in situ using a confocal Raman spectrometer (Horiba LabRam HR) with an argon laser of 488 nm wavelength to identify $CaCO_3$ polymorphs (amorphous $CaCO_3$, vaterite and calcite) at Raman shifts ranging from 200 to 1600 cm^{-1}.

2.5. Pore-scale model simulation

The OpenFOAM software was used to simulate the velocity field in the unique porous pattern (Fig. 1e) using python packages (e.g., porespy (Gostick et al., 2019) and skimage (Van der Walt et al., 2014)) to generate the spatial domains for the simulations from the microsystem images, and Gmsh (Geuzaine and Remacle, 2009) as a mesh generator. We have made this framework available in a Github repository, with detailed instructions for installation and examples. The open-source imaged-based framework for computational fluid dynamics on microsystems and details on the numerical simulations presented in this study can be found in https://github.com/daavid00/pymm.git.

3. Results

3.1. Characterization of precipitate morphologies

The precipitation of calcium carbonate is a combination of nucleation, crystal growth, and changes of the crystal polymorphs (Van Paassen, 2009). According to Ostwald's step rule, the least-stable amorphous $CaCO_3$ (ACC) forms first, then transforms to a vaterite (spherical crystal) and finally to a stable calcite (rhombohedral crystal) (Rodriguez-Blanco et al., 2011). Raman spectra peaks for precipitates indicate that three $CaCO_3$ polymorphs precipitated during our MICP experiments (Fig. 2). Shortly after CS injection (0.1 PVs) all observable precipitates were confirmed by Raman Spectroscopy to be ACC precipitates. Over time the ACC crystallized to form small vaterite particles, that subsequently transformed to calcite, consistent with previous studies (Singh et al., 2015; Wang et al., 2021). After crystal growth in the pore for 20 h, most of crystals were calcite (90% among the 38 samples in different positions).

3.2. Crystallization of calcium carbonate in a pore

Single pore MICP dynamics (Fig. 3) was studied during $CaCO_3$ precipitation via the uratolytic pathway. The $CaCO_3$ precipitation and crystallization process (Fig. 3, image series) initiated with irregular-shaped ACC precipitates forming immediately after the CS injection. The ACC precipitates grew until a spherical $CaCO_3$ crystal nucleated in the pore. The crystal nucleation started at the location with the lowest velocity (red star). This phenomenon was also observed in the entire porous pattern (Figure S3), where most crystals formed during injection of CS were located in low velocity regions. The nucleated crystal was surrounded by a precipitate-free zone (PFZ) (Kawano et al., 2002), caused by transition of $CaCO_3$ morphologies from ACC to vaterite or calcite during the nucleation and crystal growth. The PFZ increased in size with crystal growth until all ACC precipitates were dissolved. The spherical $CaCO_3$ crystal continued to grow with a declining rate towards nearby pores with less flow resistance. The crystal growth rate declined
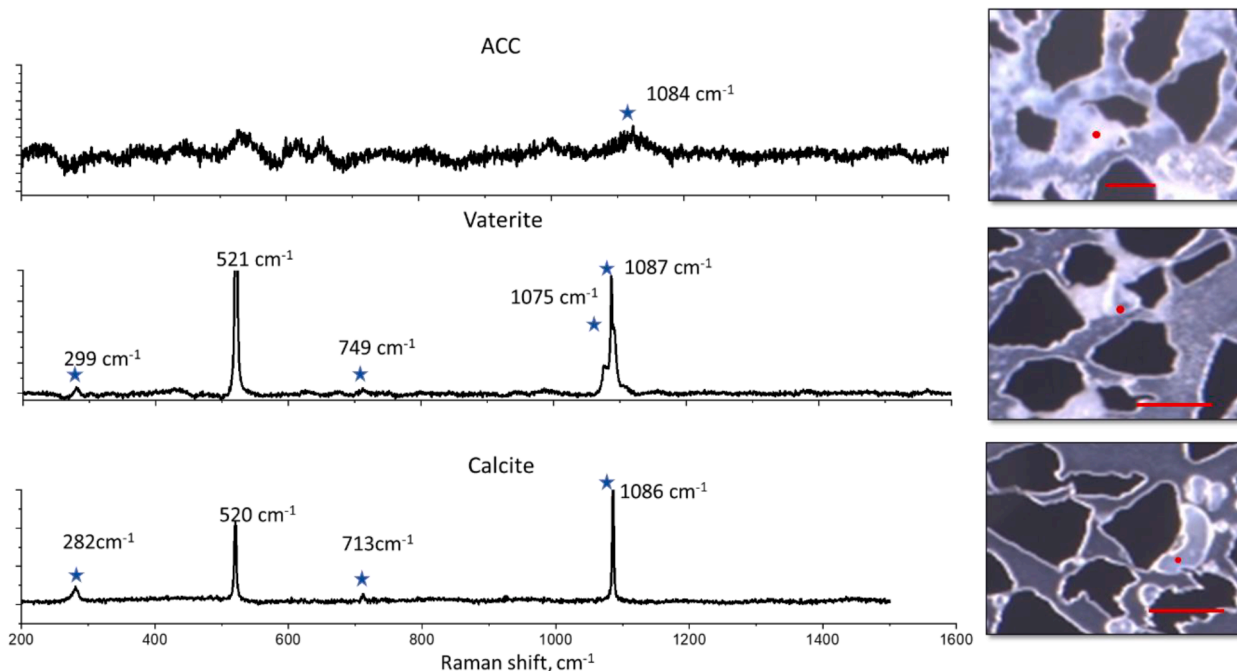

Fig. 2. Raman spectra of ACC, vaterite and calcite peaks consistent with published Raman spectra (Agarwal and Berglund, 2003; Zambare et al., 2020): peak at 1084 cm^{-1} corresponds to ACC; peaks at 299, 749, 1075, and 1087 cm^{-1} correspond to vaterite; peaks at 282, 713, and 1086 cm^{-1} correspond to calcite. The peaks at ~520 cm^{-1} correspond to the silicon surface of the microfluidic device. The red dots in right images are Raman test positions. Scale bar = 200 μm. Note that the Raman analysis was performed at ambient pressure and temperature.
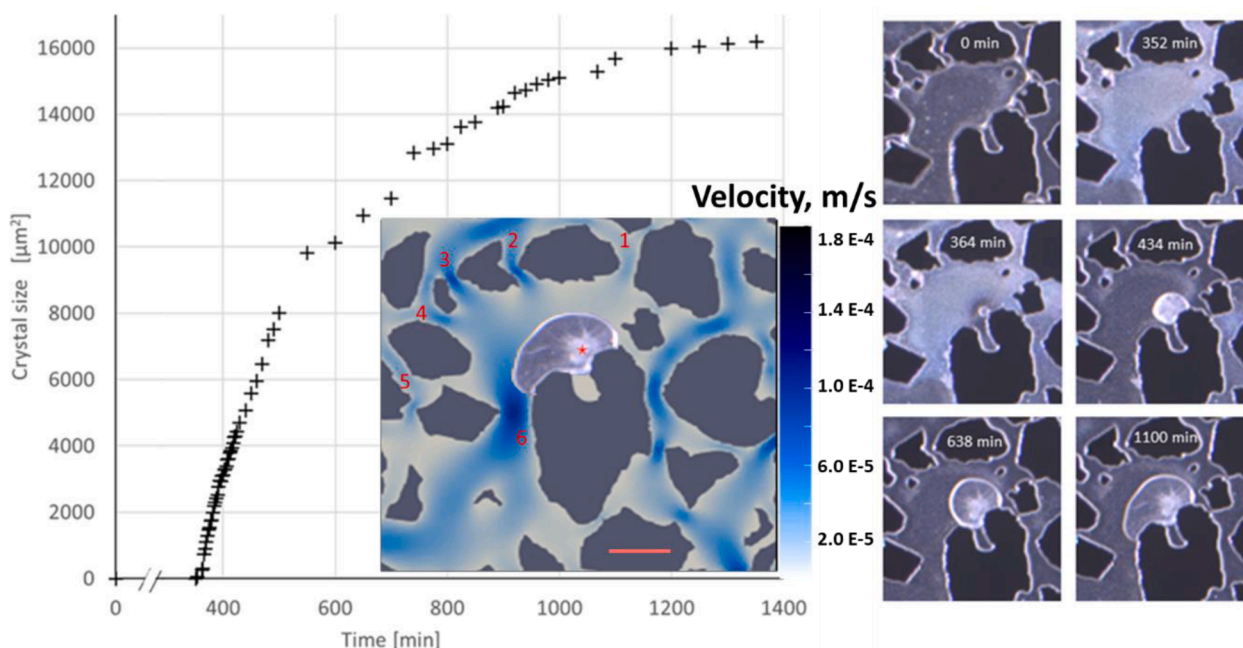
Fig. 3. Plot of CaCO$_3$ crystal size over time in a single pore at 30 °C and 19 bar. The crystal size (2D horizontal area) was measured from high-resolution images of the pore over time, with measurement uncertainty less than 0.1%. Note a break on x-axis. <u>Inset</u>: Simulated velocity field (without crystal) with OpenFOAM. The crystal is overlain velocity image for clarity and grows towards regions with less resistance (pore throat 6). Scale bar = 100 μm. <u>Image series</u>: ACC precipitates (appear as white floc) formed immediately (0 min) after start of CS injection (total 100 min of injection). The ACC precipitates grew until a spherical CaCO$_3$ crystal nucleated (364 min). The crystal growth rate was approximately 55 μm^2/min until 480 min, and declined over time until a pseudo-steady state was reached after 1000 min. The size of the precipitate-free zone increased with crystal growth until all ACC precipitates were dissolved (638 min). The spherical CaCO$_3$ crystal continued to grow towards nearby pores with less flow resistance (1100 min).

over time (from 54.93 μm^2/min down to 13.82 μm^2/min after 8 h) and reached a pseudo-steady state after 1000 min.

3.3. Spatiotemporal crystal distribution and porosity reduction

Growth of calcium carbonate crystals can reduce the porosity of the pore network, and the spatiotemporal crystal distribution was therefore quantified (Fig. 4) using the unit area (cf. Chapter 2.2). During experiments, there were no or few biofilms forming in the pore network. Initially (0–300 min) the majority of crystals (> 5 crystals per unit area) nucleated close to the inlet (upper left, port 1). Over time (> 300 min) crystals formed throughout the whole pore network, but the inlet nucleated more crystals (17% of all crystals) throughout the experiment (1200 min). The mean crystal unit size was largest (25,820 μm^2) in the outlet (lower right, port 4), but with a relatively low crystal number (3 crystals per unit area) – with an opposite size-frequency correlation compared to the inlet (Figure 4; compare left and middle columns). The outlet crystal growth rate was approximately 39 μm^2/min throughout the experiment, 4 times higher compared with the middle region and 2.6 times higher than the inlet. The pore space without crystal growth was homogenous because of the repeated porous pattern (cf. Fig. 1), and the spatially variable crystal growth rate resulted in the heterogeneous distribution of crystals in the pore network. Local porosity in inlet area decreased by up to 11% in the first 300 min (Fig. 4, right column). Over time, the porosity in inlet and outlet areas with high cementation concentrations reduced up to 21%, and high cell number areas near port 2 and port 3 also observed a porosity reduction. Plots in Figure S4 show that the crystal growth rate was 82 crystals per 100 min, and reached the maximum number at 600 min. Crystal mean size and porosity reduction demonstrate a linear relationship with crystals growth time. Differences in crystals size and number in the pore network likely result from the competition of nucleation and growth processes, where the initial nucleation rate was faster than the crystal growth rate resulting in increased crystal number while crystal growth was the key process after

600 min inducing increased crystal size.

3.4. Porous media CaCO$_3$ crystal growth kinetics

3.4.1. Effect of pore pressure

Pressure-induced ACC crystallization was observed with increasing pore pressure (ambient to 30 barg), assisting ACC dehydration for calcite (or vaterite) crystallization (Fig. 5, row I), consistent with the literature (Bots et al., 2012). We observed the effect of increased pore pressure on crystal size and number in the pore network: the mean crystal size (ambient pressure: 1053 μm^2) increased at increasing pore pressure (30 barg: 4598 μm^2), but the number of crystals decreased (Fig. 5, row II). Ambient conditions resulted in a uniform distribution with small crystal sizes, whereas at 30 barg most of large crystals grew in the outlet area. Experiments conducted at subsurface pressure (100 barg), with identical injection protocol, formed only a few crystals along the diagonal line from port 1 to port 4 because of the low bacterial activity due to pressure changes during the bacterial inoculation.

3.4.2. Effect of bacterial and cements concentrations

After preculturing, mixtures of NS and BS (10%, 50% and 100% of BS) were inoculated in the pore space, followed by 2 h of initial attachment. The effect of bacterial concentration on crystal growth was investigated by injecting 1.5 PVs of CS using the same volumetric flow rate and results are presented in Fig. 6 (blue and green symbols). The number of crystals using 100% BS (OD$_{600}$ = 0.89) was higher (2437) compared with 50% BS (OD$_{600}$ = 0.64) which formed 687 crystals. The mean size for 100% BS (4177 μm^2), however, was much smaller compared with 7031 μm^2 for 50% BS. The high bacterial concentration results in a fast crystal nucleation rate. Crystals did not form at 10% BS (OD$_{600}$ = 0.20), indicating that the low cell concentration could not induce the precipitation of CaCO$_3$. The crystal size, frequency and porosity reduction were studied as a function of pore volumes CS injected. Crystal size decreased with increasing pore volumes CS
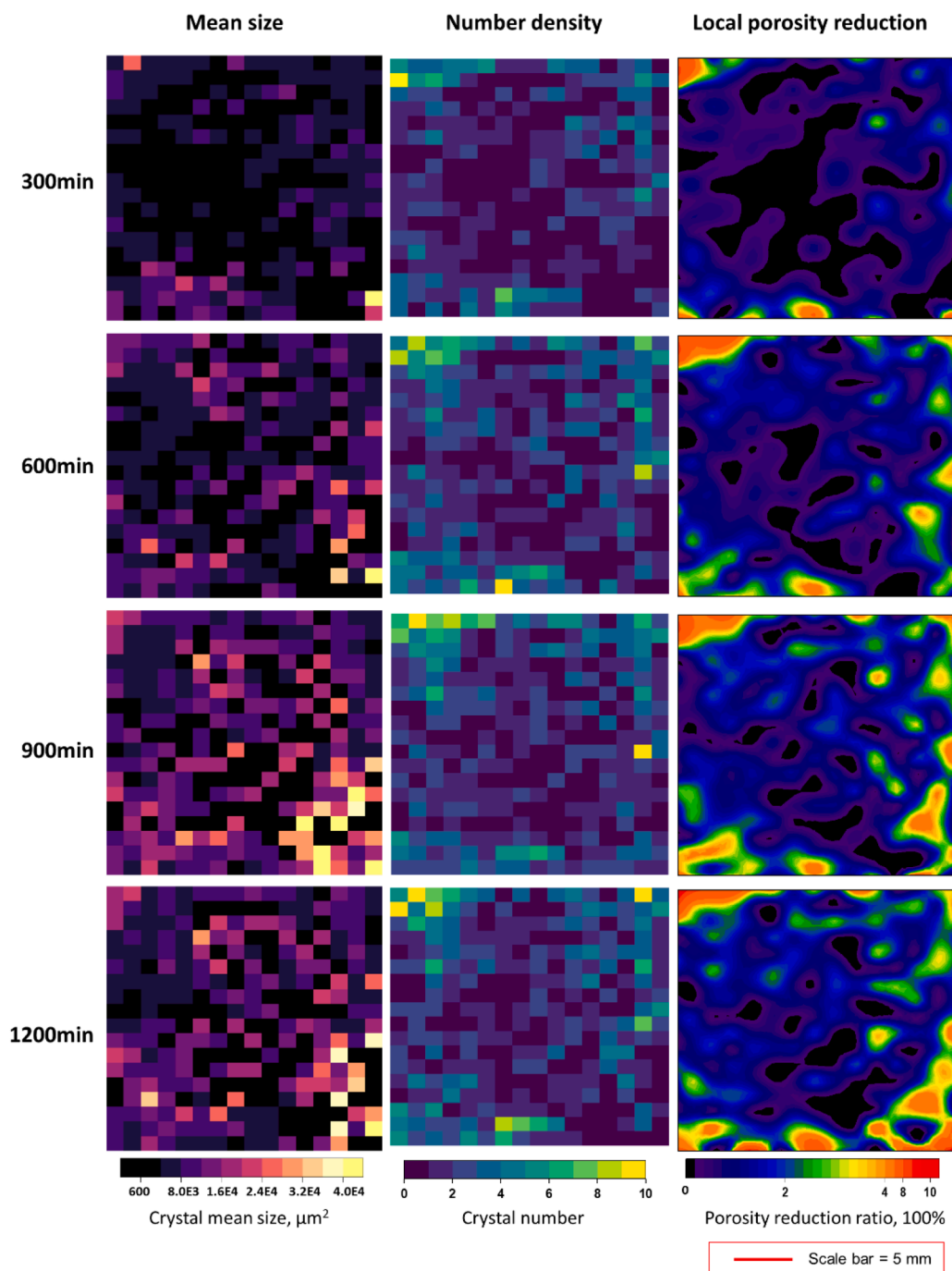
Fig. 4. Heatmaps of crystal mean size and number (left and middle columns) in each unit and contour plots of porosity reduction ratio (right column) during crystal growth at 30 °C and 19 bar. The crystal mean size initially ($\leq$ 300 min) was larger closer to the inlet (upper left) compared to other regions. Over time, crystal sizes near outlet were the largest. The crystal number in each unit reveals that most crystals nucleated in the inlet area initially, and over time crystals formed throughout the entire pore network. Hence, the outlet area (lower right) has large crystal size but low crystal number, whereas the inlet area has the highest crystal number but relatively small size (corresponds to the distribution map in Figure S5). To illustrate the porosity changes more clearly, contour lines in plots of porosity reduction were smoothed with a parameter of 9.84 E-4 and the color distribution was not linear.

injected, whereas crystal frequency declined. The porosity reduction linearly increased with the logarithm of injected PVs.

4. Discussion

MICP is essential for various environmental applications, and is a compounded and coupled biogeochemical process involving microbial growth, microbial induced urea hydrolysis, crystal nucleation and growth, and transformation of the crystal polymorphs. Hence, the MICP implementation at large scales must be carefully tailored to achieve the intended environmental remediation or mitigation. Our high-pressure, rock-on-a-chip technology observed laboratory pore-scale mechanisms of microbial-induced $CaCO_3$ precipitation and crystallization processes in the pore network. The crystal size, frequency and distribution were

analyzed, and the effects of hydrodynamics and supersaturation on the efficiency of the MICP treatment were quantified through image processing. Physicochemical and biological factors including system pressure, concentration of cementation reagents, and cell numbers were systematically evaluated for their influences on crystals growth and nucleation in porous media.

4.1. Crystal polymorphs

We observed that unstable ACCs formed after the mixing of CS and BS, and dissolved easily with the formation of $CaCO_3$ crystals, consistent with previous observations (Haugen et al., 2021; Wang et al., 2019). Calcite was the main polymorph of $CaCO_3$ precipitations after approximately 20 h of crystal growth. Amongst all the polymorphs (ACC,
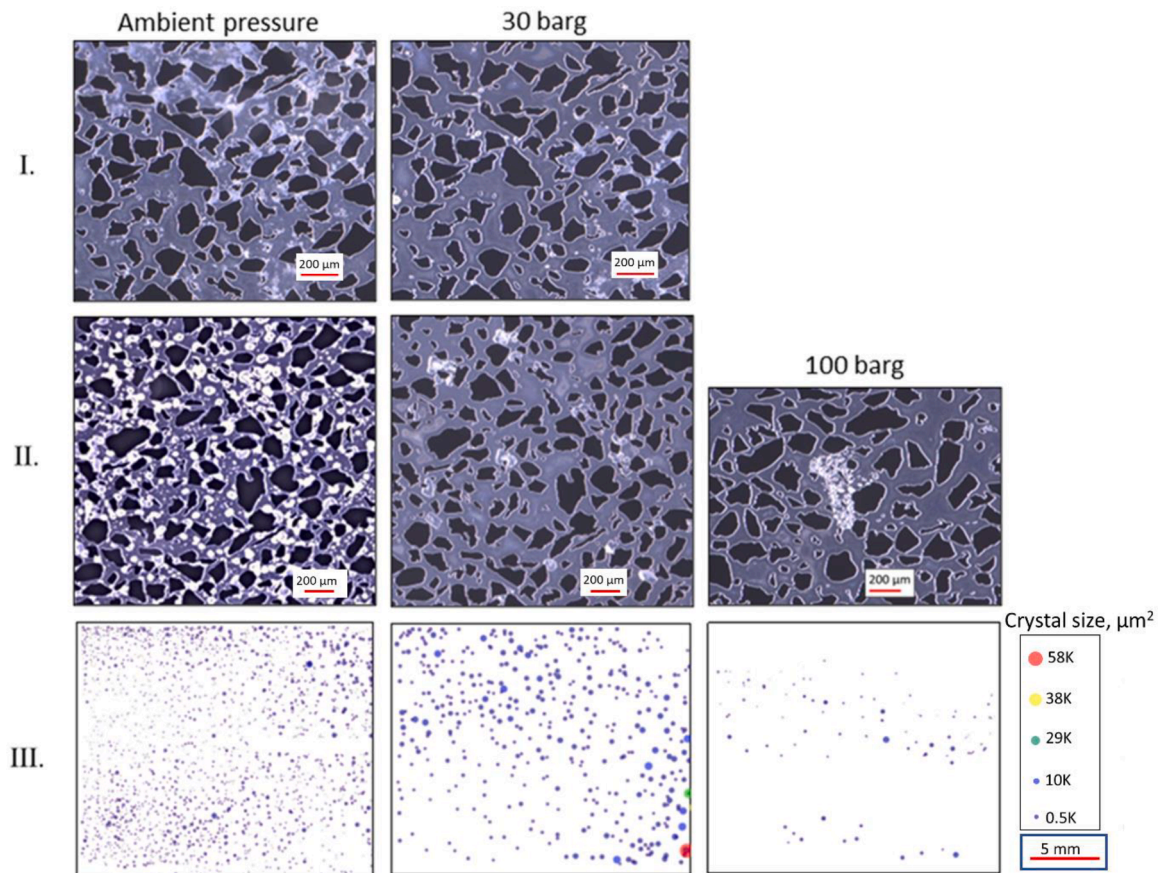
Fig. 5. The effect of pore pressure on the carbonate crystallization process. Row I: Images of the pressure-inducted crystallization process at 30 °C with ACC precipitates pressurized from ambient to 30 barg. Row II: Detailed distribution of crystals at ambient pressure, 30 and 100 barg. White spots in images of rows I and II are the CaCO3 precipitates. Row III: Crystals distribution in the pore network at different pressures. In the image processing, crystals with size less than 30 pixels (574 μm2) were not included.

vaterite and calcite), calcite is the most thermodynamically stable and desirable polymorph of calcium carbonate for engineering applications (Boulos et al., 2014). Calcite precipitations by *Sporosarcina pasteurii* has been tested at field applications to successfully enhance wellbore integrity and greatly reduce risks by leakage during CO_2 geological storage (Cunningham et al., 2011; Phillips et al., 2016).

4.2. Effect of hydrodynamics on crystal nucleation and growth

Local pore-scale hydrodynamics strongly influenced the nucleation and growth of crystals, with nucleation predominantly occurring in locations with low velocity and high bacterial cell number (Fig. 3 and Figure S3). Bacteria in the pore was displaced by the injected CS (Wang et al., 2021, 2019), and the residual cell number was influenced by the local flow velocities, where the high shear stress induced by CS flow can cause bacteria detachment (Liu et al., 2019). Because bacterial cell number has a direct effect on urease production and nucleation site (Lauchnor et al., 2015; Wang et al., 2021), the hydrodynamics in the pore determines the position of crystal nucleation and its growth. The local pore structure protects bacterial cells attached to surfaces with low shear stress and serve as nucleation sites for crystal growth. The crystal growth rate declined over time, consistent with previous observations (Yoon et al., 2019, 2012). The decrease in growth rate relates to decreased ureolytic activity of cells caused by the encapsulation of CaCO3 precipitate on cell surface (Murugan et al., 2021). Crystal growth rate was also influenced by decreased reactant concentrations (Ca^{2+} and CO_3^{2+}) during the chemical reaction of CaCO3 precipitation as the CS injection stopped after 100 min.

The inlet area of the pore network has more crystal nucleation compared to other regions, and the outlet has a faster growth rate (Fig. 4). The variation in crystals size and number results from the effect of local hydrodynamics on the nucleation and growth of crystals in the pore network. In the beginning of CS injection (< 100 min), the injected calcium ion (Ca^{2+}) reacted with carbonate ion (CO_3^{2+}) from microbial induced urea hydrolysis and formed ACC precipitates in the inlet. The high cell number provides nucleation sites that induced more crystal nucleation in the inlet compared to other regions, indicating that the nucleation process dominated the crystal growth. The chemical reaction in the inlet reduced the Ca^{2+} concentration downstream, resulting in lower crystal number in the middle and outlet. The outlet has the fastest growth rate due to the high cementation concentration and fewer crystals, which increases the growth rate of crystal mean size. Additionally, the outlet has more exposure to the external environment containing BS and CS, allowing more reactants to reach the crystal growth environment. Hence, the high bacterial concentration facilitates crystal nucleation, and the high cementation concentration promotes the crystal growth. A fast crystal growth in inlet area reduced local porosity, and, consequently, leads to injectivity loss, which should be avoided in large-scales implementations.

4.3. Effect of supersaturation on crystal size and distribution

According to the classical nucleation theory, the supersaturation is one of the key parameters to determine the kinetics of nucleation and growth of CaCO3 crystals in porous media (Wallace et al., 2013). The supersaturation is defined as the difference between the concentration of

CaCO$_3$ in the solution and its solubility, where the supersaturation ratio (S) can be calculated by the following equation (Morse, 2018; Zehner et al., 2021):

$$S = \sqrt{\frac{\left(a_{CO_3^{2-}}\right)\left(a_{Ca^{2+}}\right)}{K}}$$

where $a_{CO_3^{2-}}$ and $a_{Ca^{2+}}$ are the activities of the carbonate and calcium ions, respectively, and K is the solubility product. The nucleation and growth are two competing processes in solution, where a low supersaturation causes a faster crystal growth rate than the nucleation rate, resulting in larger crystal size and lower crystal number. At the higher supersaturation, crystal nucleation dominates the kinetics of crystal growth, resulting in larger crystals number and smaller size. Experimentally, we control the activity of carbonate ion $a_{CO_3^{2-}}$ through the BS concentration in the pore space and $a_{Ca^{2+}}$ through the amount of PVs of CS injected. Furthermore, the CaCO$_3$ solubility (K) varies with the system pressure and temperature. Hence, determining parameters for the supersaturation ratio (S) are directly linked to operating conditions (pore pressure, bacterial cell numbers and injected CS PVs) that allow for a systematic and controlled investigation of crystal size and distribution in porous media.

4.3.1. The effect of pore pressure on the solubility product K

The pore pressure can influence the crystal size by affecting the supersaturation of the solution. When the pore pressure increases, the CaCO$_3$ solubility in water increases (i.e., high solubility product, K), resulting in reduced supersaturation (Coto et al., 2012). We observed the effect of decreased supersaturation at 30 barg: the crystal size increased and crystal number decreased with increased pore pressure, consistent with our hypothesis that the low supersaturation at high pressure generates fewer and larger crystals. Only a few crystals precipitated at subsurface pressure (100 barg) due to the low bacterial activity. Even though previous studies at core scale experiments (Phillips et al., 2016; Verba et al., 2016) showed limited adverse effect from elevated pressure on the microbial (*Sporosarcina pasteurii* stains) activity, it is reported elsewhere that a rapid pore pressure increase may reduce the microbial activity (Considine et al., 2008; Sehrawat et al., 2021) to produce urease for the MICP process. Hence, our pore-scale observation indicates that MICP by *Sporosarcina pasteurii* can occur at subsurface pressure, but also demonstrate that large-scale injection protocols must carefully be evaluated in the laboratory to account for kinetics that control microbial activity and local CaCO$_3$ crystal growth.
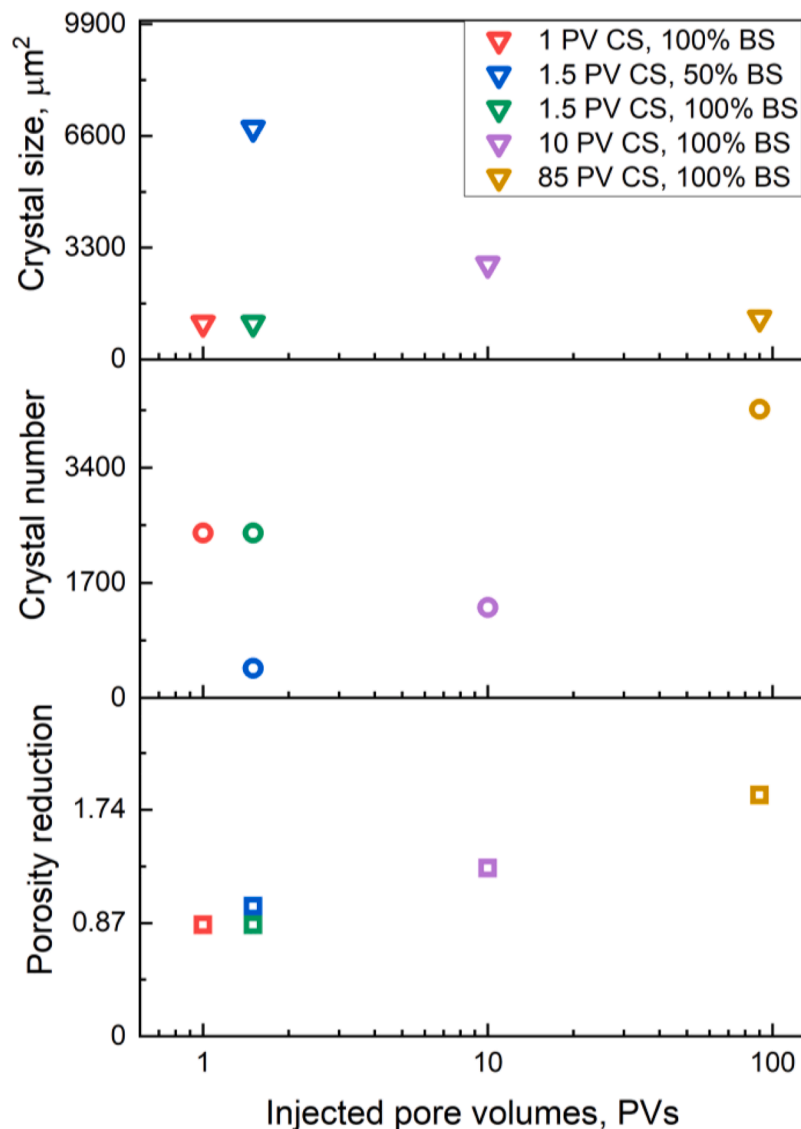

Fig. 6. Effects of bacterial cell numbers and cementation concentration on crystal growth and porosity reduction. The smallest crystal size was induced by injecting 1 PV of CS (100% BS inoculation), but many crystals nucleated, whereas 1.5 PVs of CS and 50% of BS generated the largest crystal size but the smallest crystal number. All the experiments were performed with a pore pressure of 27 barg and 30 °C, with a constant volumetric injection rate of 1 μL/min and a Ca^{2+} concentration = 0.5 M.

4.3.2. Relationship between crystal growth and size for determining parameters $a_{CO_3^{2-}}$ and $a_{Ca^{2+}}$

Bacterial concentration of the injected BS determines the total cell number, the number of nucleation sites and urease production for the $CaCO_3$ precipitation (Hammes, 2002). Hence, the bacterial concentration is directly linked to the activity of the carbonate ions ($a_{CO_3^{2-}}$) during MICP. The relationship with mean crystal size and activity of carbonate ions was reversed (Fig. 6). Hence, larger $a_{CO_3^{2-}}$ (higher bacterial cell numbers) cause a high supersaturation where the crystal nucleation rate is faster than the crystal growth rate, where high availability of cell numbers can not only offer more nucleation sites for crystal nucleation but also cause a high supersaturation.

The availability of soluble calcium ions ($a_{Ca^{2+}}$) and urea concentration in the solution is directly proportional to the injected amount of CS. The observed nonmonotonic trend (Fig. 6) shows the importance of local $a_{CO_3^{2-}}$ and $a_{Ca^{2+}}$ values as the injected CS displaced BS that reduced the bacterial cell numbers resulting in low urease production and fewer nucleation sites. Therefore, the activity level of calcium ($a_{Ca^{2+}}$) is a key factor that determines MICP efficiency by controlling the crystal size and number in porous media. This result also confirms our observation that high bacterial concentration benefits crystal nucleation, and that high cementation concentration promotes crystal growth. Improving the precipitation efficiency (ratio of $CaCO_3$ precipitates with injected raw materials) is essential for increasing the MICP performance and reducing costs of raw materials. In many studies, a pulse injection of BS and CS (Ebigbo et al., 2012; Hommel et al., 2015; Kirkland et al., 2017) was applied to increase crystals uniformity and MICP efficiency. In our work, medium bacterial concentration (50% BS) and 1.5 PVs of cementation injection generated the best performance efficiency, where the ratio of porosity reduction and injected materials (bacteria and urea) is highest.

5. Conclusions

For geological CO_2 sequestration, laboratory characterization of $CaCO_3$ nucleation and growth kinetics in porous media is essential: to maintain injectivity, MICP should deposit smaller crystals in the near wellbore region, whereas for mitigation of gas leakage pathways larger crystals should form in faults and fractures (potential leakage pathways) for improved seal performance. When applying the MICP technology for subsurface fracture sealing, high velocity in fractures and faults induces the growth of large crystals, thus sealing potential leakage pathways and improving wellbore integrity and environmental safety for carbon sequestration. Large-scale injection protocols can be designed to kinetically control crystal nucleation and growth in desired places through hydrodynamics and supersaturation in porous media. In this study, experimental results correspond qualitatively with the precipitation kinetic theory and can be used for validation of upscaled models: not only improve the fundamental understanding of the MICP process in general, but also describes a correlation between the pore-scale properties of biomineral precipitation and porosity reduction. Hence, we believe our results to be a valuable contribution towards successful implementation of MICP technology at Darcy- and field-scale geological CO_2 storage applications.

CRediT authorship contribution statement

Na Liu: Investigation, Methodology, Writing – original draft. **Malin Haugen:** Conceptualization, Methodology, Writing – original draft. **Benyamine Benali:** Methodology, Data curation. **David Landa-Marbán:** Software. **Martin A. Fernø:** Writing – review & editing, Supervision, Project administration.

Declaration of Competing Interest

The authors declare that they have no known competing financial interests or personal relationships that could have appeared to influence the work reported in this paper.

References

Agarwal, P., Berglund, K.A., 2003. Situ monitoring of calcium carbonate polymorphs during batch crystallization in the presence of polymeric additives using Raman spectroscopy. Cryst. Growth Des. 3, 941–946.

Armstrong, R., Ajo-Franklin, J., 2011. Investigating biomineralization using synchrotron based X-ray computed microtomography. Geophys. Res. Lett. 38.

Benali, B., Føyen, T.L., Alcorn, Z.P., Haugen, M., Gauteplass, J., Kovscek, A.R., Fernø, M. A., 2022. Pore-scale bubble population dynamics of CO2-foam at reservoir pressure. Int. J. Greenhouse Gas Control 114, 103607.

Bots, P., Benning, L.G., Rodriguez-Blanco, J.-D., Roncal-Herrero, T., Shaw, S., 2012. Mechanistic insights into the crystallization of amorphous calcium carbonate (ACC). Cryst. Growth Des. 12, 3806–3814.

Boulos, R.A., Zhang, F., Tjandra, E.S., Martin, A.D., Spagnoli, D., Raston, C.L., 2014. Spinning up the polymorphs of calcium carbonate. Sci. Rep. 4, 3616.

Buchgraber, M., Al-Dossary, M., Ross, C.M., Kovscek, A.R., 2012. Creation of a dual-porosity micromodel for pore-level visualization of multiphase flow. J. Pet. Sci. Eng. 86-87, 27–38.

Celia, M.A., Bachu, S., Nordbotten, J.M., Gasda, S.E., Dahle, H.K., 2005. Quantitative estimation of CO2 leakage from geological storage: analytical models, numerical models, and data needs. Greenhouse Gas Control Technologies 7. Elsevier, pp. 663–671.

Considine, K.M., Kelly, A.L., Fitzgerald, G.F., Hill, C., Sleator, R.D., 2008. High-pressure processing – effects on microbial food safety and food quality. FEMS Microbiol. Lett. 281, 1–9.

Coto, B., Martos, C., Peña, J.L., Rodríguez, R., Pastor, G., 2012. Effects in the solubility of CaCO3: experimental study and model description. Fluid Phase Equilib. 324, 1–7.

Cunningham, A., Class, H., Ebigbo, A., Gerlach, R., Phillips, A.J., Hommel, J., 2018. Field-scale modeling of microbially induced calcite precipitation. Comput. Geosci. 23, 399–414.

Cunningham, A.B., Gerlach, R., Spangler, L., Mitchell, A.C., Parks, S., Phillips, A., 2011. Reducing the risk of well bore leakage of CO2 using engineered biomineralization barriers. Energy Procedia 4, 5178–5185.

Cunningham, A.B., Lauchnor, E., Eldring, J., Esposito, R., Mitchell, A.C., Gerlach, R., Phillips, A.J., Ebigbo, A., Spangler, L.H., 2013. Abandoned well CO2 leakage mitigation using biologically induced mineralization: current progress and future directions. Greenhouse Gases 3, 40–49.

Cunningham, A.B., Phillips, A.J., Troyer, E., Lauchnor, E., Hiebert, R., Gerlach, R., Spangler, L., 2014. Wellbore leakage mitigation using engineered biomineralization. Energy Procedia 63, 4612–4619.

Ebigbo, A., Phillips, A., Gerlach, R., Helmig, R., Cunningham, A.B., Class, H., Spangler, L. H., 2012. Darcy-scale modeling of microbially induced carbonate mineral precipitation in sand columns. Water Resour. Res. 48.

Geuzaine, C., Remacle, J.-F., 2009. Gmsh: a 3-D finite element mesh generator with built-in pre-and post-processing facilities. Int. J. Numer. Methods Eng. 79, 1309–1331.

Gostick, J.T., Khan, Z.A., Tranter, T.G., Kok, M.D., Agnaou, M., Sadeghi, M., Jervis, R., 2019. PoreSpy: a python toolkit for quantitative analysis of porous media images. J. Open Source Softw. 4, 1296.

Grisak, G., Pickens, J., Cherry, J., 1980. Solute transport through fractured media: 2. Column study of fractured till. Water Resour. Res. 16, 731–739.

Hammes, F., 2002. Key roles of pH and calcium metabolism in microbial carbonate precipitation. Rev. Environ. Sci. Biotechnol. 1, 3–7.

Haugen, M., Benali, B., Føyen, T., Song, W., Fernø, M.A., Brattekås, B., 2021. Calcite-functionalized micromodels for pore-scale investigations of CO2 storage security. In: The 35th International Symposium of the Society of Core Analysts.

Hommel, J., Lauchnor, E., Phillips, A., Gerlach, R., Cunningham, A.B., Helmig, R., Ebigbo, A., Class, H., 2015. A revised model for microbially induced calcite precipitation: improvements and new insights based on recent experiments. Water Resour. Res. 51, 3695–3715.

Hu, X., Liu, X., Qiao, L., Zhang, S., Su, K., Qiu, Z., Li, X., Zhao, Q., Yu, C., 2021. Study on the spatial distribution of ureolytic microorganisms in farmland soil around tailings with different low-field NMR. Environ. Sci. Technol. 51, 1537–1543.

Jimenez-Martinez, J., Nguyen, J., Or, D., 2022. Controlling pore-scale processes to tame subsurface biomineralization. Rev. Environ. Sci. Bio/Technol. 21, 27–52.

Kawano, J., Shimobayashi, N., Kitamura, M., Shinoda, K., Aikawa, N., 2002. Formation process of calcium carbonate from highly supersaturated solution. J. Cryst. Growth 237-239, 419–423.

Kirkland, C.M., Zanetti, S., Grunewald, E., Walsh, D.O., Codd, S.L., Phillips, A.J., 2017. Detecting microbially induced calcite precipitation in a model well-bore using downhole low-field NMR. Environ. Sci. Technol. 51, 1537–1543.

Landa-Marbán, D., Tveit, S., Kumar, K., Gasda, S.E., 2021. Practical approaches to study microbially induced calcite precipitation at the field scale. Int. J. Greenhouse Gas Control 106, 103256.

Lauchnor, E.G., Topp, D.M., Parker, A.E., Gerlach, R., 2015. Whole cell kinetics of ureolysis by Sporosarcina pasteurii. J. Appl. Microbiol. 118, 1321–1332.

Lin, H., Suleiman, M., Brown, D., 2020. Investigation of pore-scale CaCO3 distributions and their effects on stiffness and permeability of sands treated by microbially induced carbonate precipitation (MICP). Soils and Foundations 60.

Liu, N., Skauge, T., Landa-Marbán, D., Hovland, B., Thorbjørnsen, B., Radu, F.A., Vik, B. F., Baumann, T., Bødtker, G., 2019. Microfluidic study of effects of flow velocity and nutrient concentration on biofilm accumulation and adhesive strength in the flowing and no-flowing microchannels. J. Ind. Microbiol. Biotechnol. 46, 855–868.

Mitchell, A.C., Dideriksen, K., Spangler, L.H., Cunningham, A.B., Gerlach, R., 2010. Microbially enhanced carbon capture and storage by mineral-trapping and solubility-trapping. Environ. Sci. Technol. 44, 5270–5276.

Mitchell, A.C., Phillips, A.J., Hiebert, R., Gerlach, R., Spangler, L.H., Cunningham, A.B., 2009. Biofilm enhanced geologic sequestration of supercritical CO2. Int. J. Greenhouse Gas Control 3, 90–99.

Morse, J.W., 2018. Chapter 7. The kinetics of calcium carbonate dissolution and precipitation. In: Richard, J.R. (Ed.), Carbonates: Mineralogy and Chemistry. De Gruyter, pp. 227–264.

Murugan, R., Suraishkumar, G.K., Mukherjee, A., Dhami, N., 2021. Insights into the influence of cell concentration in design and development of microbially induced calcium carbonate precipitation (MICP) process. PLoS ONE 16, e0254536.

Nasvi, M., Ranjith, P., Sanjayan, J., 2013. The permeability of geopolymer at down-hole stress conditions: application for carbon dioxide sequestration wells. Appl. Energy 102, 1391–1398.

Okyay, T.O., Nguyen, H.N., Castro, S.L., Rodrigues, D.F., 2016. CO2 sequestration by ureolytic microbial consortia through microbially-induced calcite precipitation. Sci. Total Environ. 572, 671–680.

Ortega-Villamagua, E., Gudino-Gomezjurado, M., Palma-Cando, A., 2020. Microbiologically induced carbonate precipitation in the restoration and conservation of cultural heritage materials. Molecules 25.

Phillips, A.J., Cunningham, A.B., Gerlach, R., Hiebert, R., Hwang, C., Lomans, B.P., Westrich, J., Mantilla, C., Kirksey, J., Esposito, R., Spangler, L., 2016. Fracture sealing with microbially-induced calcium carbonate precipitation: a field study. Environ. Sci. Technol. 50, 4111–4117.

Phillips, A.J., Lauchnor, E., Eldring, J., Esposito, R., Mitchell, A.C., Gerlach, R., Cunningham, A.B., Spangler, L.H., 2013. Potential CO2 leakage reduction through

biofilm-induced calcium carbonate precipitation. Environ. Sci. Technol. 47, 142–149.

Rodriguez-Blanco, J.D., Shaw, S., Benning, L.G., 2011. The kinetics and mechanisms of amorphous calcium carbonate (ACC) crystallization to calcite, via vaterite. Nanoscale 3, 265–271.

Sehrawat, R., Kaur, B.P., Nema, P.K., Tewari, S., Kumar, L., 2021. Microbial inactivation by high pressure processing: principle, mechanism and factors responsible. Food Sci. Biotechnol. 30, 19–35.

Siddique, R., Chahal, N.K., 2011. Effect of ureolytic bacteria on concrete properties. Construct. Build. Mater. 25, 3791–3801.

Singh, R., Yoon, H., Sanford, R.A., Katz, L., Fouke, B.W., Werth, C.J., 2015. Metabolism-induced CaCO3 biomineralization during reactive transport in a micromodel: implications for porosity alteration. Environ. Sci. Technol. 49, 12094–12104.

Song, W., Ogunbanwo, F., Steinsbo, M., Ferno, M.A., Kovscek, A.R., 2018. Mechanisms of multiphase reactive flow using biogenically calcite-functionalized micromodels. Lab Chip 18, 3881–3891.

Stocks-Fischer, S., Galinat, J.K., Bang, S.S., 1999. Microbiological precipitation of CaCO3. Soil Biol. Biochem. 31, 1563–1571.

Van der Walt, S., Schönberger, J.L., Nunez-Iglesias, J., Boulogne, F., Warner, J.D., Yager, N., Gouillart, E., Yu, T., 2014. scikit-image: image processing in Python. PeerJ 2, e453.

Van Paassen, L.A., 2009. Biogrout, ground improvement by microbial induced carbonate precipitation.

Verba, C., Thurber, A., Alleau, Y., Koley, D., Colwell, F., Torres, M., 2016. Mineral changes in cement-sandstone matrices induced by biocementation. Int. J. Greenhouse Gas Control 49, 312–322.

Wallace, A.F., Hedges, L.O., Fernandez-Martinez, A., Raiteri, P., Gale, J.D., Waychunas, G.A., Whitelam, S., Banfield, J.F., De Yoreo, J.J., 2013. Microscopic evidence for liquid-liquid separation in supersaturated CaCO3 solutions. Science 341, 885–889.

Wang, Y., Soga, K., DeJong, J., Kabla, A., 2021. Effects of bacterial density on growth rate and characteristics of microbial-induced CaCO3 precipitates: particle-scale experimental study. J. Geotech. Geoenviron. Eng. 147.

Wang, Y., Soga, K., Dejong, J.T., Kabla, A.J., 2019. A microfluidic chip and its use in characterising the particle-scale behaviour of microbial-induced calcium carbonate precipitation (MICP). Géotechnique 69, 1086–1094.

Watson, T.L., Bachu, S., 2009. Evaluation of the potential for gas and CO2 leakage along wellbores. SPE Drilling Completion 24, 115–126.

Weinhardt, F., Deng, J., Hommel, J., Vahid Dastjerdi, S., Gerlach, R., Steeb, H., Class, H., 2022. Spatiotemporal distribution of precipitates and mineral phase transition during biomineralization affect porosity–permeability relationships. Transp. Porous Media 143, 527–549.

Yoon, H., Chojnicki, K.N., Martinez, M.J., 2019. Pore-scale analysis of calcium carbonate precipitation and dissolution kinetics in a microfluidic device. Environ. Sci. Technol. 53, 14233–14242.

Yoon, H., Valocchi, A.J., Werth, C.J., Dewers, T., 2012. Pore-scale simulation of mixing-induced calcium carbonate precipitation and dissolution in a microfluidic pore network. Water Resour. Res. 48.

Zaitoun, A., Tabary, R., Rousseau, D., Pichery, T.R., Nouyoux, S., Mallo, P., Braun, O., 2007. Using Microgels to Shut Off Water in a Gas Storage well, International Symposium On Oilfield Chemistry. Society of Petroleum Engineers.

Zambare, N.M., Naser, N.Y., Gerlach, R., Chang, C.B., 2020. Mineralogy of microbially induced calcium carbonate precipitates formed using single cell drop-based microfluidics. Sci. Rep. 10, 17535.

Zehner, J., Røyne, A., Sikorski, P., 2021. Calcite seed-assisted microbial induced carbonate precipitation (MICP). PLoS ONE 16, e0240763.